The Journal of Chemical Physics

RESEARCH ARTICLE | OCTOBER 22 2026

A cross-species comparison of excitation energy transfer in red-lineage photosystem I

Ankit Pandey ; Ruibin Liang

Check for updates

J. Chem. Phys. 165, 165101 (2026)
https://doi.org/10.1063/5.0352441

View Online
Export Citation

Articles You May Be Interested In

Long-range energy transport in photosystem II
J. Chem. Phys. (June 2016)

On wavelength-dependent exciton lifetime distributions in reconstituted CP29 antenna of the photosystem II and its site-directed mutants
J. Chem. Phys. (February 2021)

Spectral densities and absorption spectra of the core antenna complex CP43 from photosystem II
J. Chem. Phys. (June 2022)

22 October 2026 18:57:08

AIP Publishing
The Journal of Chemical Physics
Special Topics Open for Submissions
Learn More

AIP Publishing

The Journal of Chemical Physics ARTICLE pubs.aip.org/aip/jcp

A cross-species comparison of excitation energy transfer in red-lineage photosystem I

Cite as: J. Chem. Phys. 165, 165101 (2026); doi: 10.1063/5.0352441
Submitted: 14 July 2026 • Accepted: 29 September 2026 •
Published Online: 22 October 2026

View Online Export Citation CrossMark

Ankit Pandey and Ruibin Liang[a)]

AFFILIATIONS

Department of Chemistry and Biochemistry, Texas Tech University, Lubbock, Texas 79409, USA

[a)]Author to whom correspondence should be addressed: rliang@ttu.edu

ABSTRACT

The photosystem I supercomplex (PSI) is a central component of photosynthesis in plants and algae. Its antenna subunits absorb light and transfer the excitation energy through an interconnected pigment network to the reaction center (RC), where it is converted to chemical energy. Although the excitation energy transfer (EET) in photosystems has been well characterized for individual organisms, evolutionary variation and inconsistent modeling settings have obscured cross-species comparisons, and it remains unclear which common structural features sustain EET efficiency. To address this, we combined kinetic modeling and rate theories to simulate EET processes in multiple red-lineage PSI complexes, each consisting of hundreds of chlorophylls, using the same set of experiment-derived parameters. We performed network analysis to probe how their EET processes respond to structural variation across distinct species. The exciton becomes increasingly delocalized as it approaches the core region of the PSI complexes. This, together with a radial site-energy bias, creates a strong exciton energy gradient (EEG) that funnels the exciton to the RC. However, the EEG is effective only over a limited distance range from the core region. In large PSI complexes, the pigments farther from the RC are weakly coupled, and the efficiency of long-range EET is maintained by additional features that complement the EEG, such as the pigment composition in the peripheral regions of the antenna, which also broadens the energy range of light absorption. By comparing red-lineage PSI complexes with a common parameter set, we provide a framework for relating EET to structural rearrangements in the pigment network.

© 2026 Author(s). All article content, except where otherwise noted, is licensed under a Creative Commons Attribution (CC BY) license (https://creativecommons.org/licenses/by/4.0/). https://doi.org/10.1063/5.0352441

22 October 2026 18:57:08

I. INTRODUCTION

The photosystem I supercomplex (PSI) is a pigment–protein assembly central to photosynthesis in plants and algae. All PSI complexes share a structurally similar central region, namely, the PSI core, which consists of two large subunits PsaA and PsaB. The core subunits bind numerous pigments that convert absorbed light into electronic excitation (excitons), which is transferred through the pigment network until it reaches the reaction center (RC) located at the interface between PsaA and PsaB.[1] The RC then uses the energy of the exciton to drive charge separation, the primary photochemical step of the light-dependent reactions of photosynthesis. Surrounding the PSI core subunits are peripheral antenna subunits that bind additional pigments, which enlarge the light-harvesting cross section and transfer excitons inward to the core subunits and ultimately to the RC.

The number of antenna subunits, their structural arrangement, and their pigment composition vary largely from species to species. In the PSI of the green lineage species (plants and green algae), the antenna is composed of light-harvesting complex *a* (Lhca) subunits that bind chlorophylls (Chl) *a* and *b*.[2] In the PSI of the red lineage species, the antenna comprises Lhcr, Lhcf, Lhcq, and RedCAP subunits that bind Chl *a* and Chl *c*.[3] Across different red-lineage species, the size of the antenna region of PSI ranges from five subunits binding slightly more than 100 pigments to more than 30 subunits binding over 500 pigments.[4–8] This structural diversity raises the question of how the trade-off between light absorption and excitation energy transfer (EET) efficiency is managed: a larger antenna captures more photons, but it also lengthens the path the excitation must travel to reach the RC,[9] increasing the probability that it is dissipated before it arrives. Nevertheless, PSI complexes from distinct species sustain quantum yields exceeding 95%.[1,6,10]

© Author(s) 2026

The structure–function relationship of PSI complexes has been studied extensively, from their overall architecture to their individual protein subunits, and both experimental and theoretical investigations of their EET processes have advanced considerably.[4–8,11,12] Recently, high-resolution structures of several red-lineage PSI complexes have been determined, including those of the unicellular red alga *Cyanidioschyzon merolae*,[7] the diatoms *Thalassiosira pseudonana*[5] and *Chaetoceros neogracilis*,[8] the haptophyte *Isochrysis galbana*,[4] and the coccolithophore *Emiliania huxleyi*.[6] In parallel, theoretical modeling of EET in photosystems has matured over the past two decades. Kinetic modeling based on a combination of Redfield and generalized Förster theories[13–16] has been applied extensively to EET in photosystems.[10,15–22] These studies enabled the visualization of EET pathways, kinetics, and bottlenecks. Such analyses have identified design principles for energy transfer in photosystems, including how excitation flows through the PSI and PSII supercomplexes[10,20,22] and why PSII employs both Chl *a* and Chl *b*.[17]

PSI complexes span a wide range of antenna sizes, and it has not been established how EET efficiency is preserved as the antenna's size changes or which structural features are shared across species to this end. Although the EET processes have been computationally modeled for individual PSI complexes using the theoretical framework described above,[10] a systematic, comparative cross-species analysis has not been reported.

To address this gap, we model EET in the red-lineage PSI complexes listed above on the basis of their recently determined high-resolution structures. Applying a single parameter set to PSI complexes from distinct species places the comparison on a common basis and separates the effects of the antenna architecture on EET from those of species-specific parameter choices: a uniform treatment fixes the model choices that influence the computed properties (such as exciton lifetimes) rather than fitting them separately for each species. Four technical choices in the EET modeling are particularly relevant: (1) the charge-separation rate constant at the RC, (2) the clustering approach that assigns pigments to delocalized exciton domains, (3) the spectral density that models the coupling of electronic excitation to the vibrational modes of the pigments and the protein environments, and (4) the site-energy landscape, which includes site energy fluctuations and variations within each protein subunit and between different subunits. Because these choices have been made independently in single-species studies, the results have been difficult to compare directly across species. Benchmarking and fixing these choices, as performed in the current study, removes this ambiguity and allows for identifying the trends across species and the common features that preserve EET efficiency.

Efficient EET to the RC relies on a so-called "funneling" or "ratcheting" mechanism that directs energy toward the core region and suppresses outward flux; otherwise, stochastic diffusion of excitons across a large antenna could lengthen the excited-state lifetime and lower the quantum yield. In previous studies, funneling has been attributed to redshifted, low-energy Chl dimers acting as gateways toward the RC[6,10] and to a gradient of site energies or exciton energies decreasing toward the core.[1,23,24]

Understanding the funneling mechanisms remain an area of active research. Site-energy differences among the pigments contribute to this mechanism, and can be classified into two categories. The first is the intra-subunit variation; the site energies of the PSI Chls have been resolved in several first-principles studies, including electrostatic and quantum-chemical calculations,[23] QM/MM molecular dynamics,[25] and polarizable QM/MM calculations.[22] The second is the inter-subunit variation, which includes a possible systematic offset between the Chls of the peripheral belts of the antenna and those of the core. Spectroscopic estimates from isolated core and antenna complexes suggest that their mean site energies may differ by several hundred cm^{-1};[10,11] however, this difference is found to be strongly attenuated in the assembled core–antenna complex.[10]

The spatial arrangement of the PSI pigments can also contribute to the funneling mechanism through a radial exciton energy gradient (EEG) that arises from variations in domains' sizes and site-couplings at different separation distances from the RC. Strong excitonic coupling and mixing with charge-transfer states can lower the exciton energy in tightly coupled Chl dimers, i.e., the so-called "red form dimers."[13,26–30] Betti *et al.*[22] reported that in plant PSI, the core subunits contains large domains of pigments where the exciton is delocalized (exciton domains), whereas the domains in the peripheral region of the antenna are smaller, and suggested that these couplings in the red-form dimers may be instrumental in trapping the excitation.[22] Whereas red form dimers are readily identified spectroscopically, it remains unclear how the varying sizes of exciton domains are spatially organized in PSI complexes with a large peripheral antenna. In particular, it remains unknown how far outward the effect of EEG on EET extends from the RC. This question is especially relevant for the larger PSI complexes, whose antenna can comprise several hundred Chls, most of which are far away from the RC, and dissipation along the extended EET pathways can reduce the quantum efficiency. Further, the inclusion of Chl *c* in addition to Chl *a* in larger antenna complexes can also alter EET substantially by reshaping the site couplings and energy landscapes. Analyzing the couplings and site energies of the peripheral pigments can, therefore, clarify how EET toward the core remains efficient as the antenna grows.

In Secs. II and III, we describe the simulations of EET and the network analyses used to address these questions.

II. COMPUTATIONAL METHODS

A. Overview

A cluster of strongly coupled pigments can form an exciton domain that delocalizes the exciton. The entire EET process can be described as a combination of coherent transitions among the eigenstates of each domain (intra-domain component) and incoherent hopping between domains (inter-domain component). The intra-domain and inter-domain EET rates are calculated with Redfield and generalized Förster theories, respectively.[17–19] These rates are then used in kinetic equations to model the time evolution of the exciton population across all exciton states in all domains following initial excitation under varying conditions. During the EET process, the total exciton population can be dissipated at pigment sites via non-radiative decay or at the RC by inducing a charge-separation reaction. The time constants of the total exciton population decay are used to characterize the exciton lifetime. The quantum yield is defined as the fraction of the initial population that has undergone charge separation at the RC by the end of the simulation. Based on the time evolution of the exciton population in each domain, network analysis is then performed to characterize the flux of exciton population between domains and to compare it across species.

22 October 2026 18:57:08

© Author(s) 2026

B. Structures of the PSI complexes

The structures of the PSI complexes of the five species studied here are taken from the following PDB entries: 5ZGB for *C. merolae*, 8ZEH for *T. pseudonana*, 6LY5 for *C. neogracilis*, 8Z11 for *I. galbana*, and 9JJ8 for *E. huxleyi*. These structures are used to compute the parameters entering the Redfield[31] and generalized Förster theories below.

C. Definition of exciton domains and belts of domains

The pigments are partitioned into exciton domains as follows. First, the Hamiltonian matrix of the whole system is constructed in the pigment-site basis, where the diagonal elements are the site energies of the pigments and the off-diagonal elements are the diabatic couplings V_{mn} between a pair of pigments in sites m and n,

$$H_{mn} = E_m\,\delta_{mn} + V_{mn}\,(1-\delta_{mn}), \tag{1}$$

where E_m is the pigment site energy of chlorophyll m, V_{mn} is the excitonic coupling between chlorophylls m and n, and δ_{mn} is the Kronecker delta. The pigment site energies E_m depend on the pigment types. The Chl *c* site energy is set to 15 786 cm^{-1} (633.4 nm).[4,32] The Chl *b* site energy, relevant only for the plant PSI-LHCI validation (Sec. III A), is set to 15 200 cm^{-1}.[33] The Chl *a* site energies are assigned by one of two treatments, both referenced to a mean core site energy of 14 800 cm^{-1}.[10] In the stepwise site-energy bias treatment (SSB) following Akhtar *et al.*,[10] all Chl *a* in the core domains share the same energy of 14 800 cm^{-1}, and the energies of the Chl *a* in the peripheral domains of the antenna are offset above the core by 65 cm^{-1} uniformly. In the binned site-energy bias treatment (BSB), the energies of the core Chl *a* are assigned using a radial-distance-based profile. Specifically, the radial distances from Chl *a* in the core domains to the midpoint of the P700 special Chl pair are calculated and binned into invervals of 10 Å, and the energy of Chl *a* in each bin is assigned a value according to the energy landscape of the plant PSI reported by Betti and Cupellini[22] The energies of Chl *a*'s not in the core domains are set to the mean value of the core domain's Chl *a* value plus 51 cm^{-1}. Table I illustrates this energy landscape derived by the BSB treatment for the plant PSI-LHCI. The BSB treatment is further discussed in Sec. III A. Static disorder is included by drawing every site energy from a Gaussian of standard deviation 100 cm^{-1} centered on these values. The two treatments, SSB and BSB, are compared in Secs. III A and III B.

TABLE I. Mean site-energy offsets of the binned site-energy bias (BSB) profile: the core domain's Chl *a* of plant PSI-LHCI are grouped based on radial distance from the midpoint of the P700 special pair, which are binned into 10 Å intervals. In each interval, the energy of Chl *a is assigned* using the site energies reported by Betti and Cupellini.[22] The first column lists the intervals of radial distances. The second column lists the number of Chl *a* per interval . The third column lists the difference between the mean energy of Chl *a* in each interval and the mean energy of all Chl *a* in the core domains.

Intervals of Radial Distances (Å)	Number of Chlorophylls	$\langle E\rangle - \langle E\rangle_{core}$ (cm^{-1})
0–10	2	−149.2
10–20	4	−76.4
20–30	14	−51.1
30–40	29	−28.7
40–50	25	+8.7
50–60	20	+46.7

The positions and orientations of pigments determine their couplings (V_{mn}). The coupling between every pair of pigments is computed from the electrostatic interaction of their transition densities with the Transition Charges from Electrostatic Potentials (TrEsp) method.[26] To do so, the transition charges are first scaled to reproduce the full Qy transition dipole strength of each chlorophyll type in the vacuum.[26,33–35] Using these transition charges and the coordinates of pigments in the PSI structure, the site couplings are calculated and then scaled down. The details of the scaling process are described in Sec. II E. The surrounding protein is treated as a dielectric continuum, and all couplings are eventually scaled by the factor $(n^2+2)^2/9n^2 = 0.889$ for a refractive index n = 1.4.[10]

After constructing the Hamiltonian in the pigment-site basis, the pigments are grouped into exciton domains following the participation-ratio clustering approach reported by Betti *et al.*[22,36,37] We use two different approaches to include site-energy disorder in the domain-partitioning process. In the first approach, we apply the same disorder-averaged domain-partitioning (described below) to each realization of the EET simulation. This is necessary for inter-domain flux network analysis since the domains need to be consistently defined for all realizations. In the second approach, each EET simulation realization has a distinct domain-partitioning pattern based on the site energies unique to that realization, and the domain partitioning varies across realizations. This domain-partitioning approach explicitly accounts for site-energy fluctuations at the domain level. All reported exciton lifetimes and quantum yields are averaged across all realizations based on the second approach. The results from these two approaches differ from each other by a few picoseconds in exciton lifetime, as shown in Table S3.

The first domain-partitioning approach is performed as follows. For every pair of pigments m and n, we compute the disorder-averaged participation ratio $PR_{mn} = \left\langle \sum_\alpha \left|c_m^{(\alpha)}\right|^2 \left|c_n^{(\alpha)}\right|^2 \right\rangle_{\rm dis}$, where $c_m^{(\alpha)}$ is the amplitude of pigment m in exciton state α of the full, unpartitioned Hamiltonian, $\left|c_m^{(\alpha)}\right|^2$ is the corresponding probability, the sum runs over all exciton states, and $\langle\cdots\rangle_{\rm dis}$ denotes an average over 500 realizations of all site energies according to Gaussian distribution (Gaussian, σ = 100 cm^{-1}). PR_{mn} is large when the two pigments repeatedly appear in the same exciton states across the ensemble and small when they do not mix. The co-participation is converted into a dissimilarity matrix, $d_{mn} = 1 - PR_{mn}/\sqrt{PR_{mm}PR_{nn}}$, which ranges from 0 for pigments that always share exciton states to 1 for pigments that never do, and the pigments are grouped by average-linkage hierarchical clustering of d_{mn}, using a fixed threshold of 0.80 for all species simulated. The resulting clusters are the exciton domains. Two constraints are imposed on the clustering: couplings between Chl *a* and Chl *c* are omitted at this step, so each domain is homogeneous in pigment type, and the two P700 chlorophylls are always assigned to one domain so that the charge-separation capacity of the reaction center is counted exactly once. With the exciton domains defined, the Hamiltonian matrix is partitioned into sub-matrices corresponding to these domains and then block-diagonalized individually. The eigenvectors and eigenvalues of each block are the exciton states $|M\rangle$ and energy levels E_M of each domain,

22 October 2026 18:57:08

© Author(s) 2026

$$|M\rangle = \sum_m c_m^{(M)} |m\rangle, \tag{2}$$

where $c_m^{(M)}$ is the expansion coefficient of exciton state $|M\rangle$ on pigment site m. The frequency of intra-domain transition between states M and N, i.e., ω_{MN}, is calculated from the energy difference between the two eigenstates.

To analyze how the antenna's spatial organization affects EET, we group the antenna subunits into concentric belts according to their distance from the conserved core region. Belt 1 contains antenna subunits that have at least one chlorophyll within 30 Å of any core chlorophyll. Belt (k + 1) contains the remaining subunits that are within 30 Å of any subunit in belt k. Figure 1 illustrates the definition of the belts of *E. huxleyi* as an example. We assign each exciton domain to the belt that contains the majority of its constituent pigments. This classification is used to analyze the dependence of EET on the distance from the core.

D. Treatment of vibronic coupling

The electronic transitions of the chlorophylls are coupled to two classes of nuclear motions: the low-frequency vibrations (phonons) and the high-frequency intramolecular vibrations of the chlorophylls. Both couplings are described by one spectral density having both low-frequency and high-frequency components, $J(\omega) = J_{ph}(\omega) + J_{vib}(\omega)$.[38,39] For the low-frequency (phonon, *ph*) component, we adopt the following Renger–Marcus form:[13]

$$J_{ph}(\omega) = \frac{1}{s_1 + s_2} \sum_{i=1,2} \frac{s_i}{2 \cdot 7! \cdot \omega_i^4} \omega^3 \exp\left[-\left(\frac{\omega}{\omega_i}\right)^{1/2}\right], \tag{3a}$$

where $s_1 = 0.8$, $s_2 = 0.5$, $\omega_1 = 0.56\ \mathrm{cm}^{-1}$, and $\omega_2 = 1.94\ \mathrm{cm}^{-1}$. The prefactor $\frac{1}{s_1+s_2}$ normalizes $J_{ph}(\omega)$, $\int_0^\infty d\omega J_{ph}(\omega) = 1$, with reorganization energy[38] $\lambda_1 = \hbar \int_0^\infty d\omega \omega J_{ph}(\omega) = 78.5\ \mathrm{cm}^{-1}$.

The high-frequency (*vib*) component consists of the discrete, localized modes of chlorophylls,

$$J_{vib}(\omega) = \sum_k S_k \delta(\omega - \omega_k), \tag{3b}$$

with frequencies ω_k and Huang–Rhys factors S_k taken from the set of modes measured for Chl *a* by differential fluorescence line-narrowing.[40] The same set of modes is used for both Chl *a* and Chl *c*. The modes below 300 cm^{-1} are removed from J_{vib} to avoid double counting, because in this range the high-frequency vibrational sideband has been reported to overlap with the low-frequency phonon sideband, and the two cannot be separated unambiguously.[41] The computed lifetimes depend only weakly on the position of this boundary: moving it between 100 and 500 cm^{-1} changes τ by less than 2%. The total vibrational Huang–Rhys factor is calculated to be $S_{vib} = \sum_k S_k = 0.344$ and the corresponding reorganization energy $\lambda_{vib} = \sum_k S_k \hbar\omega_k = 359.8\ \mathrm{cm}^{-1}$.

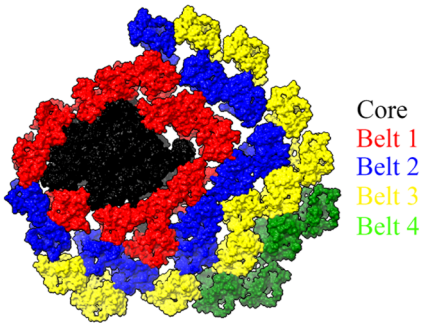


FIG. 1. Definitions of belts across the PSI subunits of *E. huxleyi*.

E. Calculations of rate constants

The rate constants for intra-domain and inter-domain EET are calculated as described in previous studies.[10,15,17–19,22] For intra-domain transitions between a pair of delocalized exciton states M and N of the same domain, we apply Redfield theory,[22,24]

$$\begin{aligned} k_{M\to N} = 2\pi\omega_{MN}^2 \sum_m \left|c_m^{(M)}\right|^2 \\ \times \left|c_m^{(N)}\right|^2 [(1 + n_{BE}(\omega_{MN}))J_m(\omega_{MN}) \\ + n_{BE}(\omega_{NM})J_m(\omega_{NM})], \end{aligned} \tag{4}$$

where $\hbar\omega_{MN} = E_M - E_N$ is the excitonic energy difference, $c_m^{(M)}$ are the expansion coefficients of Eq. (2), n_{BE} is the Bose–Einstein distribution at room temperature (T = 300 K), and J_m is the spectral density of pigment m, defined only for positive frequencies ($J_m(\omega) = 0$ for $\omega < 0$). The site-energy fluctuations of different pigments are taken to be uncorrelated; in this limit, exciton relaxation occurs only between states that share amplitude on the same pigments.[22,24] The spectral density of each pigment is[10]

$$J_m(\omega) = S_m J_{ph}(\omega), \tag{5}$$

where J_{ph} is the unit-normalized phonon spectral density of Eq. (3a) and S_m is the Huang–Rhys factor of pigment m. Based on a previous study,[10] we assign $S_m = 0.5$ to all chlorophylls, except for $S_m = 1$ assigned to the two chlorophylls of the P700 special pair.

Here, the intra-domain Redfield rates of Eq. (4) are calculated using the low-frequency phonon component of the spectral density alone; the contributions from the high-frequency intramolecular vibrational modes enter only the inter-domain line shapes.[39] The rate of transfer from exciton state M_a of donor domain a to state N_b of acceptor domain b ($a \neq b$) is given by

$$k_{M_a\to N_b} = \frac{2\pi}{\hbar^2} |V_{M_aN_b}|^2 \int d\omega\, F_{M_a}(\omega)\, A_{N_b}(\omega), \tag{6}$$

where $V_{M_aN_b} = \sum_{m_a,n_b} c_{m_a}^{(M_a)} c_{n_b}^{(N_b)} V_{m_an_b}$ is the coupling strength between the exciton states of the two domains. The integral is the spectral overlap of $F_{M_a}(\omega)$, the fluorescence line shape function of the donor state, with $A_{N_b}(\omega)$, the absorption line shape function of the acceptor state. We detail the terms entering the line shape functions as follows:[10,13,17,18]

$$A_{N_b}(\omega) = \frac{1}{\pi} \mathrm{Re} \int_0^\infty dt e^{i\left(\omega - \tilde{\omega}_{N_b}\right)t - g_{N_b}(t) - \Gamma_{N_b}t}, \tag{6a}$$

$$F_{M_a}(\omega) = \frac{1}{\pi} \mathrm{Re} \int_0^\infty dt e^{i\left(\omega - \tilde{\omega}_{M_a}\right)t - g_{M_a}^*(t) - \Gamma_{M_a}t}, \tag{6b}$$

22 October 2026 18:57:08

© Author(s) 2026

where the asterisk denotes complex conjugation. Each line shape is specified by three quantities: its effective center frequency $\tilde{\omega}_M$, its lifetime broadening Γ_M, and its line-broadening function $g_M(t)$. Both line shapes are normalized. For each exciton state, the emission line shape differs from the absorption line shape only by the complex conjugation of $g_M(t)$, which makes it the mirror image of the absorption line shape about $\tilde{\omega}_M$—the sideband lies below the center frequency in emission and above it in absorption. Following previous work,[10,22] the effective center frequency is the excitonic energy corrected for the reorganization of the bath and for the dispersive part of the exciton–phonon self-energy; the corresponding effective energy is defined as[10]

$$\tilde{E}_M = \hbar\tilde{\omega}_M = E_M - \lambda_M + \Delta_M, \tag{6c}$$

where E_M is the excitonic energy. The reorganization shift λ_M and the dispersive shift Δ_M entering it are

$$\lambda_M = \lambda_1 \sum_m \left|c_m^{(M)}\right|^4 S_m, \tag{6d}$$

where $\lambda_1 = 78.5\ \mathrm{cm}^{-1}$ is the phonon reorganization energy at the unit Huang–Rhys factor as defined after Eq. (3a), and S_m is defined in Eq. (5). In addition,

$$\Delta_M = \hbar\sum_{N\neq M}\sum_m \left|c_m^{(M)}\right|^2\left|c_m^{(N)}\right|^2 S_m\ .\mathcal{P}\int d\omega \frac{\Phi(\omega)}{\omega_{MN}-\omega}, \tag{6e}$$

where $\mathcal{P}$ denotes the Cauchy principal value, and $\Phi(\omega) = \omega^2[1+n_{BE}(\omega)]J_{ph}(\omega)$ for $\omega > 0$, while $\Phi(\omega) = \omega^2 n_{BE}(-\omega)J_{ph}(-\omega)$ for $\omega < 0$.

Γ_M is obtained from the intra-domain Redfield rates of Eq. (4) out of that state, as in previous studies:[10,17]

$$\Gamma_M = \frac{1}{2}\sum_{N\neq M} k_{M\to N}. \tag{6f}$$

Both line shapes are constructed from a single line-broadening function, in which the phonon and intramolecular components enter with different weights,[39]

$$g_M(t) = \sum_m \left|c_m^{(M)}\right|^4 S_m\ g_{ph}(t) + g_{vib}(t), \tag{6g}$$

$$g_{ph}(t) = \int_0^\infty d\omega J_{ph}(\omega)\left(\coth\left(\frac{\hbar\omega}{2k_BT}\right)[1-\cos\omega t] + i\sin\omega t\right), \tag{6h}$$

$$g_{\mathrm{vib}}(t) = \sum_k S_k\left\{\coth\left(\frac{\hbar\omega_k}{2k_BT}\right)[1-\cos\omega_k t] + i\sin\omega_k t\right\}. \tag{6i}$$

The effective scaling of S_m's in Eq. (6g) by the expansion-coefficient factor applies only to the low-frequency, delocalized phonon modes. The vibronic transitions of the high-frequency intramolecular modes are treated as localized on the individual pigment, so these modes retain full molecular Huang–Rhys factors and are not scaled.[39,42,43] This treatment follows the complex Redfield scheme with localized vibrations (cR loc. vib.) proposed by Saraceno *et al.*[44] In particular, the line shapes of Eqs. (6d)–(6h) follow their cR approach. Equation (6i) follows their loc. vib. approach for the localized high-frequency vibrational modes, which are excluded from the calculation of Redfield rates in Eq. (4) and the dispersive shift in Eq. (6e).

The Qy 0–0 band's transition dipole strength is reduced by vibronic coupling to high-frequency modes. In the calculation of the inter-domain rate constants [Eq. (6)], since the formalism explicitly accounts for the high-frequency modes, the couplings need to reflect the full transition dipole strength and should not be scaled. Thus, the transition charges needed for calculating these couplings are parameterized to represent the full transition dipole strengths of the pigments in the vacuum, which are scaled up from the measured transition dipoles strengths of the Qy 0–0 band by a factor of $e^{S_{vib}}$: $\mu^2_{\mathrm{Chl}a} = 21.0e^{S_{vib}}D^2 = 29.6\ D^2$ for Chl *a* and $\mu^2_{\mathrm{Chl}c} = 8.4e^{S_{vib}}D^2 = 11.9\ D^2$ for Chl *c*.[42,44] During the construction of the full Hamiltonian matrix [Eq. (1)], the couplings calculated from the transition charges representing the full-strength transition dipoles are scaled down by a factor of $e^{-S_{vib}}$ (~0.709), in accordance with the loc. vib. approach.

The spectral overlap in Eq. (6) is expanded as

$$k_{M_a\to N_b} = \frac{2|V_{M_aN_b}|^2}{\hbar^2}\mathrm{Re}\int_0^\infty dt e^{i\left(\tilde{\omega}_{M_a}-\tilde{\omega}_{N_b}\right)t - g_{M_a}(t) - g_{N_b}(t) - \left(\Gamma_{M_a}+\Gamma_{N_b}\right)t}. \tag{6j}$$

The Redfield and generalized Förster rates are not constructed from the same equilibrium condition. The Redfield rates of Eq. (4) satisfy detailed balance with respect to the raw excitonic energies E_M. The generalized Förster rates of Eq. (6) would satisfy detailed balance with respect to the effective excitonic energies $\tilde{E}_M$ of Eq. (6c), except that the lifetime broadening Γ_M in their line shapes is symmetric in the transition frequency and contributes equally to the high-energy and the low-energy member of each donor-acceptor pair. The rate matrix, therefore, satisfies neither condition exactly. To enforce detailed balance, for the forward and backward rate constants between each pair of exciton states [as described by Eq. (4) for intradomain transfer or Eq. (6) for inter-domain transfer], the rate for the energetically downhill direction is retained and the rate for the energetically uphill direction is reconstructed from the former using a Boltzmann factor,[22]

$$k_{M\to N} = k_{N\to M}e^{-\left(\tilde{E}_N-\tilde{E}_M\right)/k_BT} \text{ for } \tilde{E}_N > \tilde{E}_M, \tag{7}$$

and the diagonal elements of the rate matrix are set so that each column sums to zero.

F. Time propagation of EET with master equations

With all exciton transfer rates defined above, the EET is propagated through time by integrating a master equation, $dX(t)/dt = KX(t)$, where $X(t)$ is the exciton population at each exciton state at time t and K is the rate matrix assembled from the intra-domain rates calculated by Eq. (4) and the inter-domain rates by Eq. (6), with detailed balance enforced as in Eq. (7). Its diagonal elements $k_{MM} = -\sum_{N\neq M} k_{NM}$ ensure that the overall exciton population is conserved in the absence of the sink sites introduced below. Integration of the master equation yields the time-dependent populations of all exciton states. The time evolution of the total exciton population is integrated to yield the exciton lifetime τ, and the quantum yield QY for charge separation is the fraction of the initial population absorbed by the charge-separation sink at $t = \infty$.

22 October 2026 18:57:08

© Author(s) 2026

Two absorbing sink states are added to the network. The first sink represents charge separation at the reaction center. Following Betti and Cupellini,[22] it is connected to the lowest exciton state of the RC domain. We adopt the charge separation rate constant $k_{CS} = 2.8\ \text{ps}^{-1}$, corresponding to the effective charge-separation time of ~1 ps from the thermally equilibrated RC domain. Reported charge-separation times range from 1 to 3 ps.[45–48] The second sink represents intrinsic non-radiative decay of any chlorophyll to its ground state (dissipative loss) with a rate constant $k_{diss} = 2.5 \times 10^{-4}\ \text{ps}^{-1}$, corresponding to a 4 ns isolated-chlorophyll lifetime.

For the validation against the plant PSI-LHCI model of Betti and Cupellini[22] (Sec. III A), the settings of that model are also tested, with $k_{CS} = 2\ \text{ps}^{-1}$, and without RC-specific reorganization energy (uniform $S_m = 0.5$) or dissipation channel.

Unless otherwise noted, the initial population of each exciton state is set proportional to its transition dipole strength, $x_{M_a}(0) \propto \left|\sum_m c_m^{(M_a)} \vec{\mu}_m\right|^2$.

G. Absorption cross section calculation

The normalized absorption cross sections are calculated from all exciton states of all domains,

$$\sigma(\omega) \propto \sum_a \sum_{M_a} |\vec{\mu}_{M_a}|^2 \omega A_{M_a}(\omega), \tag{8}$$

where $\vec{\mu}_{M_a} = \Sigma_{m_a} c_{m_a}^{(M_a)} \vec{\mu}_{m_a}$ is the transition dipole moment of the exciton state M_a, and $A_{M_a}(\omega)$ is the absorption line shape of Eq. (6a).

H. Network analysis

After the EET has been simulated with the master equation, the time-dependent domain populations and the inter-domain EET fluxes are analyzed by network analysis. Time-integrated cumulative flow parameters are defined to track the EET pathways through which the exciton is transferred to the RC.

The directional cumulative flow from domain i to domain j is defined as $F_{ij} = \sum_{M\in i} \sum_{N\in j} k_{M\to N} \int_0^\infty X_M(t)\mathrm{d}t$,[22] where the sums run over the exciton states of the two domains, $k_{M\to N}$ are the inter-domain transfer rates of Eq. (6), and $X_M(t)$ is the population of exciton state M. Because the master equation is linear, the time-integrated populations are obtained analytically as $\int_0^\infty X(t)\mathrm{d}t = -K^{-1}X(0)$, so the flows are evaluated at full convergence of the EET dynamics. The product $k_{M\to N}\int_0^\infty X_M(t)\mathrm{d}t$ is the expected number of $M \to N$ transfers over the entire dynamics.

To delineate the net directional transport pathways, the bidirectional gross flows between each pair of domains are taken into account. To this end, the net cumulative flow (NCF) between the domain pair i,j is defined as the absolute difference between their gross forward and backward fluxes: $\text{NCF}(i,j) = |F_{ij} - F_{ji}|$. The resulting flow is assigned the direction of the larger gross flux. Selecting the links with the largest NCF values yields the major transport pathways that route exciton from the peripheral region of the antenna to the RC.

To identify the bottleneck and hub domains through which energy is routed, the cumulative input (CI) is computed for each domain j as the sum of its net incoming flows, $CI_j = \sum_{i\neq j} \max(F_{ij} - F_{ji}, 0)$.[22] Domains with large CI values are hubs located on the primary EET pathways.

I. Model assumptions and species selection

To enable a consistent comparison of PSI supercomplexes differing in antenna size, the "red form" chlorophylls of PSI are not modeled explicitly for the following reasons. Red forms arise from the interaction between the lowest excitonic transition of closely packed Chl *a* dimers and their charge-transfer states.[22,28–30] Both defining properties of the red forms follow from this admixture: the transition energy shifts to the red, and, through the static dipole of the charge-transfer configuration, the coupling to the protein environment increases, giving the mixed state a reorganization energy well above that of standard Chl *a* and making it a deeper trap than the energy shift alone implies.[49] A rigorous treatment of red forms, therefore, requires the explicit inclusion of the charge-transfer states in the Hamiltonian, with their own, much stronger bath coupling,[22,29] which is beyond the scope of our model.

A second assumption is that the PSI complexes retain their state under normal light conditions. Extreme low- or high-light conditions can substantially alter PSI lifetimes; under high light, this behavior has been ascribed a photoprotective role.[50] Analogous photoprotective quenching is well characterized in the antenna complexes of PSII.[36,51,52] Under such conditions, some antenna subunits have also been proposed to decouple physically from the core.[50] Such abnormal states would confound a comparison intended to isolate the effect of antenna size on EET. The cross-species comparison is, therefore, restricted to species whose PSI, under normal light conditions, is reported to contain no low-energy exciton traps in the pigment network's energy landscape. For example, the diatom *T. pseudonana* has been reported to lack the long-wavelength Chls typical of plants and cyanobacteria;[10,53] the antenna sink of *C. neogracilis* (reported as *C. gracilis*) has been described as shallow;[54] for *E. huxleyi* the antenna landscape is reported to be flat and free of energy traps;[6] and for the "medium-light" preparation of *C. merolae*, no long-wavelength Chl pools were detected in the antenna.[50]

III. RESULTS AND DISCUSSION

A. Radial site energy gradient in the PSI complexes

To compare the EET processes across species on the same footing, it is crucial to design a method to treat the PSI's site-energy landscape consistently for all species. To this end, we first analyzed the landscapes reported in the literature and found that some of them exhibit a monotonic radial decrease in site energy toward the P700 special pair. Building upon a recently reported energy landscape by Betti and Cupellini[22] for PSI-LHCI, we designed the BSB treatment (detailed in Sec. II C) to consistently construct the energy landscape for all red-lineage PSI complexes studied here. First, we analyzed the site energies reported by Betti and Cupellini[22] for the plant PSI-LHCI. We renormalized these site energies so that the mean core Chl *a* site energy equals 14 800 cm^{-1}, and then binned them according to their radial distances to the midpoint of the P700 special pair with 10 Å intervals. The energy reference (zero) is set to the mean site energy of the Chl *a* in the core. The mean energy of Chl *a* in each distance interval is observed to decrease monotonically as it approaches the P700 special pair (Table I) in this benchmark system.

In the BSB treatment of the PSI complexes in the current study, following the binning process, the site energy of each core-domain Chl *a* in a distance interval was assigned the mean value of the

22 October 2026 18:57:08

© Author(s) 2026

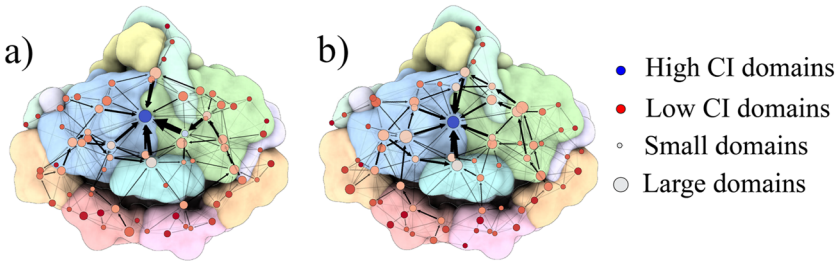


FIG. 2. (a) Network analysis of plant PSI-LHCI with the site-energy landscape deposited by Betti and Cupellini.[22] (b) The same analysis with the coarse-grained landscape built from the 10 Å binned values of Table I. Symbol size is proportional to domain size, arrow thickness to the NCF magnitude, and color to the cumulative input (CI) of each domain.

Chl *a* energies inthis interval reported by Betti and Cupellini.[22] The site energy of each Chl *a* outside the core domains was assigned to be 51 cm^{-1} above the mean energy of the core domains. This core–antenna offset is close to the 50 cm^{-1} used by Akhtar *et al.* in their structural model of diatom PSI; their estimate of about 65 cm^{-1} is the value adopted in the SSB treatment (Sec. II C).[22] Thus, the BSB treatment coarse-grained the energy landscape reported by reported by Betti and Cupellini[22] for the plant PSI-LHCI, consistently generating energy landscapes for all red-lineage PSI complexes studied here.

To benchmark the BSB treatment of energy landscape, we compared the network analysis results obtained from this approach with that obtained from the original energy landscape reported by Betti and Cupellini.[22] In both cases, the exciton flux converges on the RC domain in the "bikewheel" pattern (Fig. 2). The domain sizes follow the expected trend, being largest near the RC in the core and smaller in the peripheral regions of the antenna. A coarse-grained landscape generated by the BSB treatment may overestimate exciton delocalization relative to the fully resolved landscape; this effect can be compensated by tightening the domain-clustering criterion, but the correction has a negligible effect on the lifetimes (see the section "Sensitivity of the exciton lifetime to the domain-clustering threshold" of the supplementary material).

Betti and Cupellini[22] reported a ring of low-energy Chls near the RC that is not captured by our 10 Å binning procedure. A finer, 5 Å binning resolves this fine feature, as well as the accessory Chls lying below P700 in energy and a local energy maximum at the adjacent A_0 chlorophylls; a similar maximum was reported by Adolphs *et al.*[23] for cyanobacterial PSI. However, these fine features have little effect on the calculated exciton lifetime, which is 35.1, 33.8, and 34.9 ps for the original landscape by Betti and Cupellini,[22] the BSB treatment using 10 Å intervals, and the same treatment using 5 Å intervals, respectively.

A similar radial decrease in site energy within the core is found upon binning the core site energies reported for the PSI of *I. galbana* by He *et al.*[4] In the latter, the P700 pair lies ~200 cm^{-1} below the mean value of Chl *a* in the antenna periphery, matching the pattern shown in Table I for the plant PSI landscape reported by Betti and Cupellini.[22] In contrast, the cyanobacterial PSI site energies reported by Adolphs *et al.*[23] and Reiter *et al.*[25] show a relatively flat surface with no significant radial site energy gradient.

We also tested the SSB treatment (Sec. II C) of site energies, which assigns one value uniformly to all Chls in the core domain and another shifted value uniformly to all Chls in the peripheral domains of the anntenna. The structural model utilized by Akhtar *et al.*[10] is the same as our SSB treatment. While this assumption might be suitable for cyanobacterial PSI landscapes, it is not as applicable to the sloped landscapes of the PSI core found in plant and *I. galbana*. On this note, the absence of a peripheral antenna in cyanobacterial PSI suggests that the sloped site-energy landscape could be a unique feature of antenna-containing PSI complexes, facilitating the energy transfer from the antenna to the core. Consequently, the conclusion by Reiter *et al.*[25] that thermal site-energy fluctuations tend to overpower the effect of a static energy funnel in the landscape,[25] which applies to cyanobacterial PSI, might not hold for PSI complexes with large antennas.

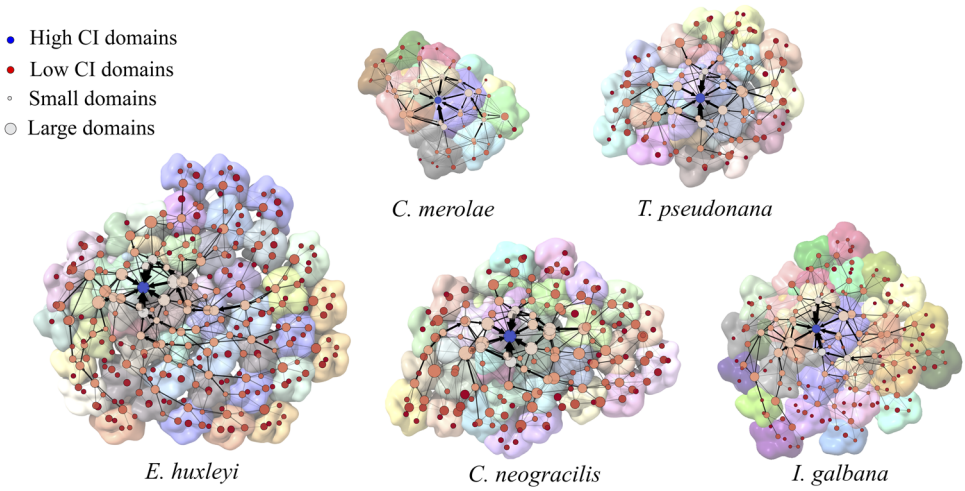


FIG. 3. Net cumulative flow (NCF) analysis of the five red-lineage PSI complexes (species labeled), showing the flow of exciton population among exciton domains. Symbol size is proportional to domain size, arrow thickness to the NCF magnitude, and color to the cumulative input (CI) of each domain over the course of the simulation (see Sec. II for definitions). The BSB landscape was utilized for these computations.

22 October 2026 18:57:08

© Author(s) 2026

Explicit evaluation of site energies using quantum mechanical treatments may help clarify the above questions. However, our current study focuses on examining how the expansion of antenna sizes across species affects EET. For our purposes, we consider it sufficient to consistently apply the energy landscapes generated by the BSB treatment (Table I) to PSIs of all species studied here and compare the resulting exciton lifetimes and quantum yields.

B. Exciton lifetimes and EET quantum yields in PSI complexes as a function of antenna size

Figure 3 presents the network analysis of the five red-lineage PSI complexes. The bikewheel pattern of exciton flow in the plant PSI-LHCI complex (Fig. 2) is observed in the PSI complexes of all five species. Also, consistent with plant PSI-LHCI the core domains have consistently larger sizes than the antenna domains in the red-lineage PSIs. This is expected considering the highly conserved subunits in the PSI core across species.[55–57]

TABLE II. Exciton lifetimes (τ) and quantum yields (QY) evaluated with SSB and BSB energy landscapes, using the RC charge-separation rate $k_{CS} = 2.8\ ps^{-1}$. These values are compared with the available experimentally measured lifetimes. The experimental values are the amplitude-weighted mean lifetimes reported for *C. merolae* and *T. pseudonana* and the slowest decay component reported for *E. huxleyi*. The standard errors from disorder averaging are below 1 ps in τ and below 0.1% in QY in all cases.

Species	τ BSB (ps)	τ SSB (ps)	τ Expt. (ps)	QY BSB (%)	QY SSB (%)
C. merolae	28	40	25–30[50]	99.3	99.0
T. pseudonana	43	60	38–42[10]	98.9	98.5
I. galbana	53	72	N/A	98.7	98.2
C. neogracilis	66	86	N/A	98.4	97.8
E. huxleyi	94	119	96–120[6]	97.7	97.0

Table II summarizes the calculated exciton lifetimes (τ) and EET quantum yields (QY) when an exciton is initially distributed across all exciton states of all exciton domains in proportion to their relative transition dipole strengths (Sec. II). The computed lifetimes are compared with experimental values wherever available. As expected, the exciton lifetime increases and the QY decreases with antenna size (Table II). For *C. merolae* and *T. pseudonana*, the BSB treatment yields results in closer agreement with the experiment than the SSB treatment.

C. The effects of exciton energy gradient (EEG) near the core region

We next examine the possible role of domain-size variations in EET efficiency across PSI species. As previously reported by Betti and Cupellini,[22] the PSI core subunits can form extended domains, indicating extensive delocalization of the exciton, while the peripheral antenna domains remain small.[22] Our calculations reproduce this contrast in all five red-lineage species. In addition, we find that the domain size difference is not confined to the core–antenna boundary: the mean exciton-domain size decreases from the core through the inner antenna belts, so that antenna subunits nearer the

TABLE III. Mean size of exciton domains (Chls per domain) per belt region, under the BSB treatment, as obtained from the disorder-averaged participation ratio (Sec. II C).

Species	Core	Belt 1	Belt 2	Belt 3	Belt 4
C. merolae	3.39	2.42	N/A	N/A	N/A
T. pseudonana	3.54	1.91	N/A	N/A	N/A
I. galbana	3.06	1.80	1.76	1.57	N/A
C. neogracilis	3.27	2.07	1.83	1.77	N/A
E. huxleyi	3.31	1.85	1.70	1.59	1.65

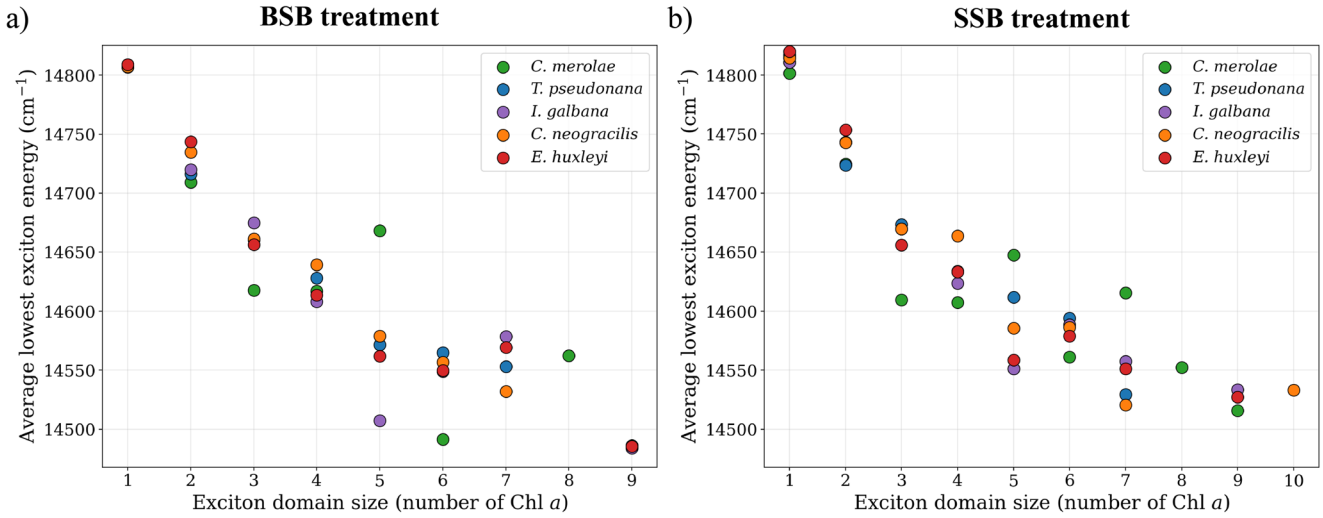


FIG. 4. Average lowest-exciton energy of a domain as a function of domain size for the five red-lineage species studied. For each species, the mean lowest-exciton energy of all Chl *a* - containing domains of each size is plotted. Larger domains have lower energies on average. The energy landscapes obtained from the (a) BSB treatment and (b) SSB treatment were utilized for these calculations.

22 October 2026 18:57:08

© Author(s) 2026

core retain larger domains than those farther out (Table III); only the outermost belt of *E. huxleyi* departs slightly from this trend.

The domain-size gradient contributes to the EEG. Excitonic coupling lowers the energy of the lowest exciton state of a domain, and the larger the number of strongly coupled pigments, the greater this effect is on average. The large core domains, therefore, can form lower-lying acceptor exciton states than the small antenna domains. Figure 4 illustrate the correlation between domain size and the mean lowest-exciton energy, obtained by averaging the energy of the lowest exciton state over all Chl *a* domains of a fixed size. It is worth noting that this trend is observed using both BSB and SSB treatments of the energy landscape. The SSB treatment uniformly assign site energies to the core-domain pigments. The correlation between lowest excitonic energy and the domain size under the SSB treatment is a strong indicator that it is the domain size itself, other than the variation in site energies along the radial direction, that largely contribute to the EEG. The domain-size gradient, therefore, contributes to an EEG in the energy landscape that funnels excitation into the core and limits the outflow of excitons toward the periphery of the antenna. The gradient is steepest at the core–antenna boundary. and persists through the inner antenna belts in the three species with more than one belt (Table III and Fig. 1).

D. Role of Chl *c* in EET and absorption spectrum

The number of Chl *c* generally increases with the size of the antenna, from none in the PSI of *C. merolae* to 152 of 563 Chls in that of *E. huxleyi*. Because the transition dipole strength of Chl *c* in the model is smaller than that of Chl *a* (11.9 D^2 vs 29.6 D^2), the coupling between Chl *c* and other Chls and among themselves are likely to be smaller on average, resulting in slower EET involving Chl *c*. Thus, as the number of Chl *c* increases, the exciton lifetime could increase. To test this hypothesis, we replaced all Chl *c* withChl *a* and recalculated the exciton lifetime and EET QYs. The results are summarized in Table IV.

Contrary to our expectation, replacing all Chl *c* with Chl *a* lengthens the exciton lifetime (Table IV), with the largest increase

TABLE IV. Effect of Chl *c* → Chl *a* substitution on the exciton lifetime τ (ps) and QY (%) using the BSB treatment.

Species	τ (native) → τ (all Chl *a*)	QY
T. pseudonana	43 → 46 (+7%)	98.9 → 98.9
I. galbana	53 → 65 (+22%)	98.7 → 98.4
C. neogracilis	66 → 73 (+12%)	98.4 → 98.2
E. huxleyi	94 → 117 (+25%)	97.7 → 97.1

observed in the largest PSIs, such as that of *E. huxleyi*, where Chl *c* accounts for 27% of the total number of Chls. This indicates that Chl *c* accelerates EET. This effect can be attributed to the higher site energy of Chl *c* than Chl *a*, which outweighs the slowing effects due to its weaker coupling. Also, this accelerating effect can be attributed to the higher abundance of Chl *c* in the peripheral belts of the antenna than the inner belts. Due to this composition differential across the antenna, the energy gradient from the high-energy Chl *c* to the low-energy Chl *a* aligns well with the direction of EET from the peripheral to inner belts of the antenna.

In addition to its role in EET, Chl *c* broadens the absorption spectra of the PSI complex, enhancing the absorption of additional photons with more blue-shifted wavelengths in optically crowded environments (Fig. 5). This is evident when comparing the contributions to the total absorption spectra from the domains containing Chl *c* with domains containing Chl *a* only (Fig. 5).

Figure 6 compares the calculated absorption spectra with the experimental spectra of *C. merolae* and *T. pseudonana*.[10,58] The computed spectra are narrower than the experimental ones because all Chls of the same type in the antenna domains are assigned the same site energies, neglecting the variations and disorder in their site energies across the subunits.

IV. CONCLUSIONS

In this study, we combined kinetic modeling, the Redfield and generalized Förster theories, and network analysis to simulate and

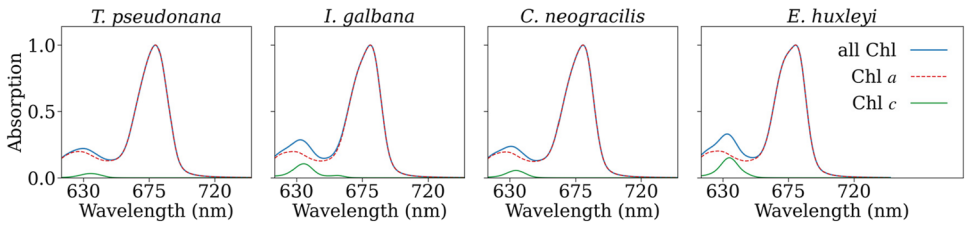


FIG. 5. Calculated absorption spectra of the four Chl *c* - containing PSI complexes (solid blue line), decomposed into the contributions from Chl *a* - containing domains (dashed red line) and Chl *c* -containing domains (solid green line).

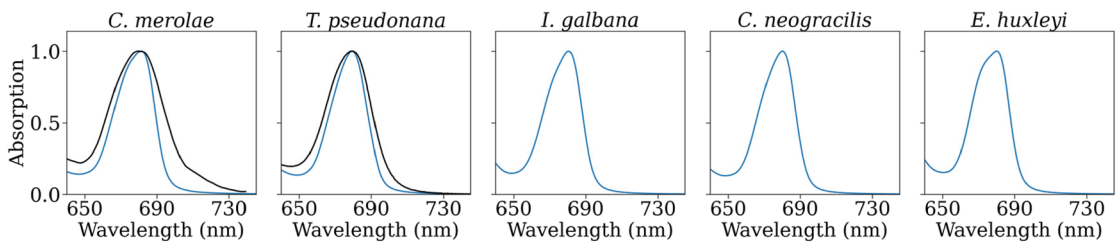


FIG. 6. Calculated absorption spectra of the five PSI complexes (blue). Experimental spectra of *C. merolae* and *T. pseudonana* (black) are compared.[10,58]

22 October 2026 18:57:08

© Author(s) 2026

compare EET across five red-lineage PSI complexes with a common parameter set. This comparison shows how the EET kinetics and quantum efficiency vary with the size, coupling, and energy landscape of the pigment network. The computed exciton lifetimes are consistent with the available experimental values. We identified structural factors that maintain EET efficiency over long transfer pathways. Large, strongly coupled pigment clusters form low-energy exciton domains in the core region due to extensive exciton delocalization, creating an EEG that funnels excitation toward the RC; the same contrast between core and peripheral antenna has been reported for plant PSI.[22] Across the red-lineage species examined here, the contrast is graded, with domain sizes decreasing as their distances from the RC increases. The EEG arises primarily from pigment packing and connectivity and does not require red-shifted Chl dimers with low site energies, which suggests that the energy landscape for EET can be tuned by the spatial arrangement of the pigments. The peripheral antenna, in contrast, consists of small, weakly coupled exciton domains containing the higher-energy Chl *c*, which enables efficient downhill antenna-to-core EET. Where the antenna extends beyond the range over which the EEG is effective, the larger PSI complexes contain an increasing proportion of Chl *c* in the peripheral antenna, which accelerates EET through fast downhill transfer of excitons into the Chl *a* network.

Although the overall exciton lifetimes increase with antenna size, all five complexes sustain average quantum yields above 97%, reflecting the effectiveness of the funneling mechanisms described above.

Several limitations of the models should be noted. As described in Sec. II I, the "red form" Chl dimers of PSI are not modeled here: they arise from mixing with charge-transfer states and feature a correspondingly larger reorganization energy, so their treatment requires explicit charge-transfer states.[22,29] Moreover, their formation is dynamic, induced under specific light conditions, often with photoprotective roles.[37,50,51,59] These effects are beyond the scope of the present study. The model also omits the carotenoids, which mediate nonphotochemical quenching (NPQ) in individual antenna complexes; these processes have been modeled explicitly in other studies.[16,22,51,60] Despite these limitations, the principles identified here may apply to other PSI complexes: the pigment network balances the competing demands of light absorption and EET through the combined effects of the domain-size variations, the site-energy bias, and the pigment composition. The computational models developed here can be applied to model EET in other red-lineage PSIs.

SUPPLEMENTARY MATERIAL

The supplementary material discusses how the domain-clustering threshold affects exciton lifetimes, along with an analysis of different excitation patterns for each PSI system in our cross-species study. Table S1 compares exciton lifetimes obtained using different domain-clustering thresholds, and Table S2 compares exciton lifetimes for the initial excitation confined to the core region and to the antenna belts. Table S3 compares the exciton lifetimes calculated with a single domain-partitioning scheme using the disorder-averaged participation ratio with those calculated with distinct domain-partitioning schemes for each instance of site-energy realization.

ACKNOWLEDGMENTS

This work was supported by the National Institutes of Health (Grant No. R35GM150780) and the Texas University Fund (TUF) for the Human Molecular Aging Center at Texas Tech University under internal Award No. TUF6656. We acknowledge the computing facilities provided by the High-Performance Computing Center at Texas Tech University. We also thank Dr. Pierre Cardol at the Université de Liège for helpful suggestions on the choice of red- and green-lineage PSI species.

AUTHOR DECLARATIONS

Conflict of Interest

The authors have no conflicts to disclose.

Author Contributions

Ankit Pandey: Data curation (lead); Formal analysis (lead); Software (lead); Writing – original draft (lead). **Ruibin Liang**: Conceptualization (lead); Funding acquisition (lead); Methodology (lead); Project administration (lead); Supervision (lead); Writing – review & editing (lead).

DATA AVAILABILITY

The data that support the findings of this study are available within the article and its supplementary material. Additional data are available from the corresponding author upon reasonable request. An example of our network analysis code is available at the following GitHub repository: https://github.com/FysicsTeachr/psi-eet.

REFERENCES

[1] M. Byrdin, I. Rimke, E. Schlodder, D. Stehlik, and T. A. Roelofs, Biophys. J. **79**, 992 (2000).
[2] Y. Mazor, A. Borovikova, I. Caspy, and N. Nelson, Nat. Plants **3**, 17014 (2017).
[3] A. Chrysafoudi, S. Maity, U. Kleinekathöfer, and V. Daskalakis, J. Phys. Chem. Lett. **12**, 9626 (2021).
[4] F.-Y. He, L.-S. Zhao, X.-X. Qu, K. Li, J.-P. Guo, F. Zhao, N. Wang, B.-Y. Qin, X.-L. Chen, J. Gao, L.-N. Liu, and Y.-Z. Zhang, Proc. Natl. Acad. Sci. U. S. A. **121**, e2413678121 (2024).
[5] Y. Feng, Z. Li, Y. Yang, L. Shen, X. Li, X. Liu, X. Zhang, J. Zhang, F. Ren, Y. Wang, C. Liu, G. Han, X. Wang, T. Kuang, J. R. Shen, and W. Wang, J. Integr. Plant Biol. **67**, 949 (2025).
[6] L. Shen, F. Ren, Y. C. Wang, Z. Li, M. Zheng, X. Li, W. Fan, Y. Yang, M. Sang, C. Liu, G. Han, S. Qin, J. Fan, L. Tian, T. Kuang, J. R. Shen, and W. Wang, Science **389**, eadv2132 (2025).
[7] X. Pi, L. Tian, H. E. Dai, X. Qin, L. Cheng, T. Kuang, S. F. Sui, and J. R. Shen, Proc. Natl. Acad. Sci. U. S. A. **115**, 4423 (2018).
[8] C. Xu, X. Pi, Y. Huang, G. Han, X. Chen, X. Qin, G. Huang, S. Zhao, Y. Yang, T. Kuang, W. Wang, S. F. Sui, and J. R. Shen, Nat. Commun. **11**, 5081 (2020).
[9] R. Croce and H. van Amerongen, Science **369**, eaay2058 (2020).
[10] P. Akhtar, Y. Feng, W. Wang, J.-R. Shen, C. Büchel, H.-S. Tan, and P. H. Lambrev, Cell Rep. Phys. Sci. **6**, 102731 (2025).
[11] P. Akhtar, W. Wang, S. Singhal, F. Sarlós, J.-R. Shen, and P. H. Lambrev, Photosynth. Res. **163**, 62 (2025).
[12] K. Kato, Y. Nakajima, R. Sakamoto, M. Kumazawa, K. Ifuku, T. Ishikawa, J.-R. Shen, A. Takabayashi, and R. Nagao, Sci. Adv. **11**, eaea6241 (2025).

22 October 2026 18:57:08

© Author(s) 2026

[13]T. Renger and R. A. Marcus, J. Chem. Phys. **116**, 9997 (2002).
[14]A. Ishizaki and G. R. Fleming, Proc. Natl. Acad. Sci. U. S. A. **106**, 17255 (2009).
[15]E. Cignoni, V. Slama, L. Cupellini, and B. Mennucci, J. Chem. Phys. **156**, 120901 (2022).
[16]C. John, L. Pedraza-González, E. Betti, L. Cupellini, and B. Mennucci, J. Phys. Chem. B **129**, 117 (2025).
[17]E. Kim, D. Lee, S. Sakamoto, J. Y. Jo, M. Vargas, A. Ishizaki, J. Minagawa, and H. Kim, Sci. Adv. **11**, eads0327 (2025).
[18]D. I. G. Bennett, K. Amarnath, and G. R. Fleming, J. Am. Chem. Soc. **135**, 9164 (2013).
[19]F. Segatta, L. Cupellini, M. Garavelli, and B. Mennucci, Chem. Rev. **119**, 9361 (2019).
[20]S. J. Yang, D. J. Wales, E. J. Woods, and G. R. Fleming, Nat. Commun. **15**, 8763 (2024).
[21]S. Maity and U. Kleinekathöfer, Photosynth. Res. **156**, 147 (2023).
[22]E. Betti and L. Cupellini, JACS Au **6**, 4513 (2026).
[23]J. Adolphs, F. Müh, M. E.-A. Madjet, M. Schmidt am Busch, and T. Renger, J. Am. Chem. Soc. **132**, 3331 (2010).
[24]T. Renger, Photosynth. Res. **102**, 471 (2009).
[25]S. Reiter, F. L. Kiss, J. Hauer, and R. de Vivie-Riedle, Chem. Sci. **14**, 3117 (2023).
[26]M. E. Madjet, A. Abdurahman, and T. Renger, J. Phys. Chem. B **110**, 17268 (2006).
[27]R. Croce and H. van Amerongen, Photosynth. Res. **116**, 153 (2013).
[28]R. Croce, A. Chojnicka, T. Morosinotto, J. A. Ihalainen, F. van Mourik, J. P. Dekker, R. Bassi, and R. van Grondelle, Biophys. J. **93**, 2418 (2007).
[29]V. Sláma, L. Cupellini, V. Mascoli, N. Liguori, R. Croce, and B. Mennucci, J. Phys. Chem. Lett. **14**, 8345 (2023).
[30]E. Wientjes, G. Roest, and R. Croce, Biochim. Biophys. Acta, Bioenerg. **1817**, 711 (2012).
[31]G. Raszewski and T. Renger, J. Am. Chem. Soc. **130**, 4431 (2008).
[32]C. Büchel, Biochim. Biophys. Acta, Bioenerg. **1861**, 148027 (2020).
[33]T. Renger, I. Trostmann, C. Theiss, M. E. Madjet, M. Richter, H. Paulsen, H. J. Eichler, A. Knorr, and G. Renger, J. Phys. Chem. B **111**, 10487 (2007).
[34]A. Mikalčiūtė, A. Gelzinis, M. Mačernis, C. Büchel, B. Robert, L. Valkunas, and J. Chmeliov, J. Chem. Phys. **156**, 234101 (2022).
[35]R. S. Knox and B. Q. Spring, Photochem. Photobiol. **77**, 497 (2003).
[36]E. Betti, L. Cupellini, and B. Mennucci, Cell Rep. Phys. Sci. **7**, 103099 (2026).
[37]P. Saraceno, V. Slama, and L. Cupellini, J. Chem. Phys. **159**, 184112 (2023).
[38]J. Adolphs and T. Renger, Biophys. J. **91**, 2778 (2006).
[39]T. Renger, M. E. Madjet, A. Knorr, and F. Müh, J. Plant Physiol. **168**, 1497 (2011).
[40]J. R. Reimers, M. Rätsep, and A. Freiberg, Front. Chem. **8**, 588289 (2020).
[41]M. Rätsep, J. Pieper, K.-D. Irrgang, and A. Freiberg, J. Phys. Chem. B **112**, 110 (2008).
[42]F. Caycedo-Soler, A. Mattioni, J. Lim, T. Renger, S. F. Huelga, and M. B. Plenio, Nat. Commun. **13**, 2912 (2022).
[43]M. Yang, A. Damjanović, H. M. Vaswani, and G. R. Fleming, Biophys. J. **85**, 140 (2003).
[44]P. Saraceno, A. Bhartiya, J. Seibt, T. Renger, T. Kramer, and L. Cupellini, J. Chem. Phys. **164**, 044119 (2026).
[45]S. Kumazaki, H. Kandori, H. Petek, K. Yoshihara, and I. Ikegami, J. Phys. Chem. **98**, 10335 (1994).
[46]S. Savikhin, W. Xu, P. Martinsson, P. R. Chitnis, and W. S. Struve, Biochemistry **40**, 9282 (2001).
[47]M. G. Müller, J. Niklas, W. Lubitz, and A. R. Holzwarth, Biophys. J. **85**, 3899 (2003).
[48]P. Akhtar, I. Caspy, P. J. Nowakowski, T. Malavath, N. Nelson, H.-S. Tan, and P. H. Lambrev, J. Am. Chem. Soc. **143**, 14601 (2021).
[49]V. I. Novoderezhkin, R. Croce, M. Wahadoszamen, I. Polukhina, E. Romero, and R. van Grondelle, Phys. Chem. Chem. Phys. **18**, 19368 (2016).
[50]M. Abram, R. Białek, S. Szewczyk, J. Karolczak, K. Gibasiewicz, and J. Kargul, Biochim. Biophys. Acta, Bioenerg. **1861**, 148093 (2020).
[51]E. Cignoni, M. Lapillo, L. Cupellini, S. Acosta-Gutiérrez, F. L. Gervasio, and B. Mennucci, Nat. Commun. **12**, 7152 (2021).
[52]L. Cupellini, S. Jurinovich, I. G. Prandi, S. Caprasecca, and B. Mennucci, Phys. Chem. Chem. Phys. **18**, 11288 (2016).
[53]A. Busch and M. Hippler, Biochim. Biophys. Acta, Bioenerg. **1807**, 864 (2011).
[54]A. Yamagishi, Y. Ikeda, M. Komura, H. Koike, K. Satoh, S. Itoh, and Y. Shibata, J. Phys. Chem. B **114**, 9031 (2010).
[55]A. Ben-Shem, F. Frolow, and N. Nelson, Nature **426**, 630 (2003).
[56]M. Antoshvili, I. Caspy, M. Hippler, and N. Nelson, Photosynth. Res. **139**, 499 (2019).
[57]A. Amunts, O. Drory, and N. Nelson, Nature **447**, 58 (2007).
[58]P. Haniewicz, M. Abram, L. Nosek, J. Kirkpatrick, E. El-Mohsnawy, J. D. J. Olmos, R. Kouřil, and J. M. Kargul, Plant Physiol. **176**, 1433 (2018).
[59]S. Akimoto, Y. Ueno, M. Yokono, J. R. Shen, and R. Nagao, Photosynth. Res. **146**, 87 (2020).
[60]D. Accomasso, G. Londi, L. Cupellini, and B. Mennucci, Nat. Commun. **15**, 847 (2024).

22 October 2026 18:57:08

© Author(s) 2026